

A typical medium cluster approach for multi-branch phonon localization

Wasim Raja Mondal,¹ Tom Berlijn,² N. S. Vidhyadhiraja,³ and Hanna Terletska^{4,*}

¹*Department of Physics and Astronomy, Middle Tennessee State University, Murfreesboro, TN 37131, USA*

²*Center for Nanophase Materials Sciences, Oak Ridge National Laboratory, Oak Ridge, Tennessee 37831, USA*

³*Jawaharlal Nehru Centre for Advanced Scientific Research, Bangalore 560 064, India.*

⁴*Department of Physics and Astronomy, Middle Tennessee State University*

(Dated: November 19, 2024)

The phenomenon of Anderson localization in various disordered media has sustained significant interest over many decades. Specifically, the Anderson localization of phonons has been viewed as a potential mechanism for creating fascinating thermal transport properties in materials. However, despite extensive work, the influence of the vector nature of phonons on the Anderson localization transition has not been well explored. In order to achieve such an understanding, we extend a recently developed phonon dynamical cluster approximation (DCA) and its typical medium variant (TMDCA) to investigate spectra and localization of multi-branch phonons in the presence of pure mass disorder. We validate the new formalism against several limiting cases and exact diagonalization results. A comparison of results for the single-branch versus multi-branch case shows that the vector nature of the phonons does not affect the Anderson transition of phonons significantly. The developed multi-branch TMDCA formalism can be employed for studying phonon localization in real materials.

I. INTRODUCTION

Anderson localization¹⁻⁴ of phonons^{5,6} has emerged as an area of great interest recently, owing to its potential for fundamental research as well as practical applications in fields such as thermoelectrics^{7,8}, phononics⁹ and beyond. For example, in thermoelectric materials, Anderson localization can serve as a mechanism to enhance thermal transport properties. Specifically, the ability to localize phonons can be used as a tool to enhance the figure of merit (zT) by reducing the contribution of phonons to thermal transport through phonon localization. For instance, the zT value of C_{60}/Cu_2Se nanocomposites has been found to increase by 20-30% compared to that of pure Cu_2Se , achieving a value of 1.4 at 773K^{7,8}. This was achieved by reducing thermal conductivity through phonon scattering and increasing the Seebeck coefficient by carrier localization, which originates from the incorporation of C_{60} nanoparticles. Very recently, Yang *et al.*¹⁰ experimentally achieved ultralow thermal conductivity (0.19 W/mK) and a record average zT (1.2 at room temperature) for $Mg_3(Sb,Bi)_2$ materials by utilizing phonon-localization. A coupled phonon-magnon localization is found to enhance function near ferroic glassy states¹¹. In the field of nanotechnology, phonon localization has been actively explored in reduced dimensions¹²⁻¹⁴ in superlattice structures, where it has been effectively used to enhance their performance and capabilities¹⁵. Despite the challenges in achieving phonon localization due to the broad spectrum of heat-carrying phonons, there have been reports of its direct observation in several technologically important materials, as well as in artificially made elastic networks. For example, Manley *et al.*¹⁶ observed ferroelectric phonon localization in relaxor ferroelectric PMN-30%PT using neutron scattering. Howie *et al.*¹⁷ observed phonon localization in a dense hydrogen-deuterium binary alloy.

Faez *et al.*¹⁸ experimentally revealed the criticality of the Anderson localization transition for phonons. Phonon localization has also been observed in a random three-dimensional elastic network¹⁹. Luckyanova *et al.*¹⁵ observed phonon localization in GaAs/AlAs superlattices in the presence of randomly distributed ErAs nanodots at the interfaces. Very recently, Islam *et al.*²⁰ found localization of optical phonon modes in boron nitride nanotubes.

All these experimental observations call for theoretical investigations of phonon localization in realistic models involving complex degrees of freedom, particularly considering the multi-branch vector nature of phonons. The direction of vibrations can have a significant impact on the Anderson transition. For example, the vector character of light may suppress Anderson localization of light, at least for point scatters²¹. However, such a prominent effect of the direction of vibrations on Anderson transition has not been found for the elastic wave considering elastic wave scattering²². The theory of elasticity is primarily concerned with continuous media and long-wavelength phenomena. In contrast, optical phonons involve discrete atomic displacements, which limits the direct applicability of elastic theory to these modes. Nevertheless, optical phonons are the most susceptible to Anderson localization, as discussed in Ref.²³. Consequently, a comprehensive investigation of Anderson localization that incorporates the microscopic atomic details of phonons is essential for understanding phonon localization.

Various numerical methods including continuum field theory⁵, diagrammatic technique²⁴, exact diagonalization^{14,25}, multifractal analysis²⁶, transfer matrix method²⁷ have been put forth to investigate the phonon localization, especially in simplified models. Alternatively, effective medium methods, such as Coherent Potential Approximation (CPA)^{28,29}. and its cluster

extensions, including the Dynamical Cluster Approximation (DCA) ^{30–36} have been used to model simple phonon systems. The random binary alloys with mass and force-constant disorder and with the vector nature of vibrations have been studied using the itinerant coherent-potential approximation (ICPA) ³⁷. However, this method in its present formalism is not able to explore the localization aspect of the phonons. Also, in this context, various first-principles-based calculations ^{38,39} have recently been utilized to study phonon localization in realistic systems.

Despite the progress, modeling, and simulation of complex realistic features responsible for phonon localization in materials remains challenging. An effective numerical method would involve constructing material-specific force-constant models and solving them. The absence of lattice translational symmetry in disordered solids and the breakdown of the Bloch theorem make this task difficult to solve straightforwardly. Moreover, force-constants calculations are computationally expensive compared to electronic case hopping calculations, and maintaining the force-constants sum rule can be challenging, especially in the presence of disorder. The inclusion of vibration directions adds another layer of complexity to the problem due to the correlations, where the vibration of an atom at site R_l in the α direction is coupled with the vibration of an atom at site $R_{l'}$ in the β direction. Furthermore, accurately capturing Anderson localization in such systems is challenging, as it often requires the calculation of two-particle transport quantities or finite-size scaling analysis that can be computationally expensive, particularly for complex realistic models. ⁴⁰

In this paper, to enable a more realistic modeling of phonon systems and their localization within the effective medium framework, we have developed the multi-branch cluster DCA and its typical medium variant, TMDCA. The DCA and TMDCA, are two cluster-effective medium methods that were originally developed for electronic systems ^{30–36}, and are used to study the disorder effects and localization, respectively. In the present work, building upon our previous work on phonon localization in a mass-disordered binary alloy using a single-direction vibration model ²³, we have extended the cluster formalism to three directions of vibrations. We validate the developed formalism against several exact diagonalization results and limiting scenarios. Applying our developed multi-branch formalism, we investigate how the vector nature of vibrations affects the spectra and localization of phonons. After comparing the results of single-branch and multi-branch situations, we found that the Anderson transition of phonons is not significantly influenced by the vector nature of the phonons for the specific model considered in this work. Overall, the present study provides further understanding of the localization of vector phonons and brings the TMDCA one step closer to being an efficient numerical tool for studying Anderson localization of phonons in materials from first principles.

The paper is organized as follows. In section II, we

describe the model, the Green's function approach we utilize to solve our problem, and provide a detailed description of our multi-branch DCA and TMDCA cluster approaches. In section III, we present our results and their discussion. We conclude in section IV.

II. FORMALISM AND MODEL

A. Hamiltonian

We consider the lattice vibrational Hamiltonian in the harmonic approximation, given as

$$H = \sum_{\alpha,i,l} \frac{(p_i^\alpha(l))^2}{2M_i(l)} + \frac{1}{2} \sum_{\alpha,\beta,l,l',i,j} \Phi_{ij}^{\alpha\beta}(l,l') u_i^\alpha(l) u_j^\beta(l'), \quad (1)$$

here $p_i^\alpha(l)$ and $u_i^\alpha(l)$ represent, respectively, the momentum and the displacement (from the equilibrium) of the i^{th} atom with mass $M_i(l)$ in a unit cell occupying the lattice site R_l vibrating along “branch” $\alpha = (x, y, z)$ directions. The index i represents the atom's number in the unit cell with N_{cell} being the maximum number of atoms in the unit cell; the index l denotes the atom position on a lattice. The force-constant $\Phi_{ij}^{\alpha\beta}(l,l')$ couples the i^{th} atom at the lattice site R_l vibrating along the α direction with the j^{th} atom at the lattice site $R_{l'}$ vibrating along the β direction. Note, that the mass $M_i(l)$ in Eq. 1 can vary randomly from site to site and, in general, can be modeled by different types of disorder distributions ²³.

B. Green's function formalism

Applying the equation of motion method to the Hamiltonian of Eq. 1, we obtain the equation for the phonon Green's function, $D_{ij}^{\alpha\beta}(l,l',\omega)$, in the following form

$$M_i(l)\omega^2 D_{ij}^{\alpha\beta}(l,l',\omega) = \delta_{\alpha\beta} \delta_{ll'} \delta_{ij} \mathbb{1} + \sum_{\gamma,l'',j'} \Phi_{ij'}^{\alpha\gamma}(l,l'') D_{j'l''}^{\gamma\beta}(l'',l',\omega), \quad (2)$$

here, $D_{ij}^{\alpha\beta}(l,l',\omega)$ is the retarded displacement-displacement phonon Green's function ²⁹, defined as

$$iD_{ij}^{\alpha\beta}(l,l',\omega) = \langle\langle u_i^\alpha(l,\omega); u_j^\beta(l',\omega) \rangle\rangle. \quad (3)$$

$\langle\langle \dots \rangle\rangle$ stands for the expectation value and time ordering between two displacement ($u_i^\alpha(l)$) and ($u_j^\beta(l')$) operators.

Eq. 2 can be rewritten in terms of the Dyson's equation using the “dressed” $D_{ij}^{\alpha\beta}(l,l',\omega)$ and “bare” non-disordered phonon Green's functions $D_{ij}^{\alpha\beta(0)}(l,l',\omega)$ as

follows

$$\left(D_{ij}^{\alpha\beta}(l, l', \omega)\right)^{-1} = \left(D_{ij}^{\alpha\beta(0)}(l, l', \omega)\right)^{-1} - \omega^2 V_{ij}^{\alpha\beta}(l, l'), \quad (4)$$

where the mass-disorder potential is given as

$$V_{ij}^{\alpha\beta}(l, l') = \left(1 - \frac{M_i(l)}{M_0}\right) \delta_{\alpha\beta} \delta_{ij} \delta_{ll'}. \quad (5)$$

Note, that the mass-disorder potential is local and identical in all directions (x, y, z), i.e., it is completely diagonal in both the branch and spatial bases.

In the zero mass-disorder limit, the mass does not vary from site to site, corresponding to $M_i(l) = M_0$, and hence the system becomes translationally invariant. In such a case, Eq. 2, when expressed in momentum \mathbf{k} -space, reduces to

$$D_{ij}^{\alpha\beta(0)}(\mathbf{k}, \omega) = \left[\omega^2 \mathbb{1} - F_{ij}^{\alpha\beta}(\mathbf{k})\right]^{-1}, \quad (6)$$

here, $F_{ij}^{\alpha\beta}(\mathbf{k})$ is related to the force-constants $\Phi_{ij}^{\alpha\beta}(l, l')$ as

$$F_{ij}^{\alpha\beta}(\mathbf{k}) = \sum_{l'} \frac{\Phi_{ij}^{\alpha\beta}(l, l')}{M_0} e^{i\mathbf{k}\cdot(\mathbf{R}_l - \mathbf{R}_{l'})}. \quad (7)$$

In our current implementation, we consider the host mass M_0 to be unity and account for one atom per unit cell considering just the nearest neighbors ($R_{l'} = R_{l\pm 1}$). Therefore, from here on, we will omit the atom indices i, j , and the host-mass index M_0 in our discussions.

C. Dynamical Cluster Approximation for multi-branch phonons

In this section, we provide a detailed description of our extension of the Dynamical Cluster Approximation (DCA) to the multi-branch phonon case. The DCA, as outlined in^{30,41}, serves as a cluster extension of the CPA method, a commonly used single-site effective medium approach employed to investigate the impact of disorder in models and materials^{28,29}. In the CPA, the original lattice problem is mapped into an impurity problem embedded in an effective medium, which is determined self-consistently. In the absence of disorder, this is equivalent to the dynamical mean-field theory for strongly correlated systems (DMFT)⁴², a well-established and powerful tool for handling many-body strong correlation effects in clean systems. The DCA, as a cluster extension of the CPA, systematically incorporates non-local spatial correlations that are absent in the CPA. These correlations have been identified as crucial for accurately describing the effects of disorder⁴³.

The DCA is a momentum-space cluster extension of the CPA, in which the original lattice with N sites is mapped onto a periodic cluster of size $N_c = L_c^d$ (L_c is

the linear dimension of the cluster, d is the dimensionality of the system) embedded into a self-consistently determined effective medium. In reciprocal space, this is equivalent to the division of the Brillouin zone of the underlying lattice into N_c cells of size $(2\pi/L_c)$, centered at the reciprocal cluster vectors \mathbf{K} .^{30,41} The lattice momenta within a given cell are denoted by $\tilde{\mathbf{k}}$. In the self-consistency loop, the DCA cluster Green's function is obtained from the \mathbf{k} -dependent lattice quantities via coarse-graining over the momenta $\tilde{\mathbf{k}}$, with $\mathbf{k} = \mathbf{K} + \tilde{\mathbf{k}}$. After disorder-averaging, the translational symmetry is restored, allowing one to use the usual lattice Fourier transform to obtain the disorder-averaged cluster quantities either from reciprocal space into real space or vice versa using the Fourier transform. The DCA algorithm recovers local CPA for $N_c = 1$, and becomes exact as $N_c \rightarrow \infty$. Therefore, with increasing the cluster size N_c , the DCA systematically interpolates between the single-site and the exact result while remaining in the thermodynamic limit. We refer the reader to Ref.^{30,41} for further details.

In the following, we describe the self-consistency numerical procedure used in our multi-branch extension of the DCA formalism. In the DCA, the effective medium is characterized by a non-local hybridization function $\Gamma(\mathbf{K}, \omega)$, which is constructed from the calculation of the disorder-averaged cluster DCA Green's function. The analysis is performed iteratively until the cluster disorder-averaged Green's function becomes the same as the coarse-grained lattice Green's function within a certain numerical accuracy. In this work, we extend the single-branch DCA phonon algorithm²³ to the multi-branch phonon system. The resulting DCA numerical self-consistently iterative procedure is described as follows:

1. We start with an initial guess of the hybridization $\Gamma_{\text{old}}^{\alpha\beta}(\mathbf{K}, \omega)$. One can start with an initial guess of the effective medium hybridization function either by setting $\Gamma_{\text{old}}^{\alpha\beta}(\mathbf{K}, \omega) = 0$ or using the coarse-grained non-disordered Green's function

$$\Gamma_{\text{old}}^{\alpha\beta}(\mathbf{K}, \omega) = \omega^2 \mathbb{1} - \frac{N_c}{N} \sum_{\tilde{\mathbf{k}}} F^{\alpha\beta}(\mathbf{K} + \tilde{\mathbf{k}}) - \left[\bar{D}^{\alpha\beta(0)}(\mathbf{K}, \omega)\right]^{-1}, \quad (8)$$

here $D^{\alpha\beta(0)}(\mathbf{K}, \omega) = \frac{N_c}{N} \sum_{\tilde{\mathbf{k}}} D^{\alpha\beta(0)}(\mathbf{K} + \tilde{\mathbf{k}}, \omega)$ is the coarse-grained bare Green's function of Eq. 6 (a bar denotes the coarse-grained quantities).

2. To set up the cluster problem, we then compute the cluster-excluded Green's function $\mathcal{D}^{\alpha\beta}(\mathbf{K}, \omega)$ of the effective medium as

$$\mathcal{D}^{\alpha\beta}(\mathbf{K}, \omega) = \left[\omega^2 \mathbb{1} - F^{\alpha\beta}(\mathbf{K}) - \Gamma_{\text{old}}^{\alpha\beta}(\mathbf{K}, \omega)\right]^{-1}. \quad (9)$$

For each cluster vector \mathbf{K} , \mathcal{D} is $N_b \times N_b$ matrix; $N_b = 3$ corresponds to three branch directions of the vibration.

3. Next, to solve the cluster problem (with the disorder distributed randomly at cluster sites L, L'), we first

Fourier transform Eq. 9 to the real-space form of the cluster

$$\mathcal{D}^{\alpha\beta}(L, L', \omega) = \sum_{\mathbf{K}} \mathcal{D}^{\alpha\beta}(\mathbf{K}, \omega) \exp^{i\mathbf{K}(\mathbf{R}_L - \mathbf{R}_{L'})}. \quad (10)$$

4. We then construct the cluster Green's function for a given disorder configuration V :

$$\begin{aligned} D^{\alpha\beta}(V, L, L', \omega) \\ = \sqrt{\mathbb{1} - V(L, L)} \left[\left[\mathcal{D}^{-1}(\omega) - \omega^2 \hat{V} \right]_{LL'}^{\alpha\beta} \right]^{-1} \sqrt{\mathbb{1} - V(L', L')}, \end{aligned} \quad (11)$$

here \mathcal{D} , D are $N_b N_c \times N_b N_c$ matrices in the real space of the cluster. In our analysis, we consider a binary alloy disorder described by the following distribution function

$$P(V(L, L)) = c_A \delta(V(L, L) - V_A) + c_B \delta(V(L, L) - V_B), \quad (12)$$

here c_A is the concentration of A atoms and $c_B = (1 - c_A)$ is the concentration of B atoms at a given cluster site L , and $V_A = -V_B$.

5. Next, we perform the averaging over disorder and calculate the disorder-averaged cluster Green's function

$$D_{ave}^{\alpha\beta}(L, L', \omega) = \left\langle D^{\alpha\beta}(V, L, L', \omega) \right\rangle, \quad (13)$$

where $\langle \dots \rangle$ indicates an averaging over disorder configurations.

6. The disorder-averaged cluster Green's function of Eq. 13 is then Fourier transformed from the real space to the momentum space $D_{ave}^{\alpha\beta}(\mathbf{K}, \omega)$ and is used to calculate the coarse-grained lattice Green's function

$$\begin{aligned} \bar{D}^{\alpha\beta}(\mathbf{K}, \omega) = \frac{N_c}{N} \sum_{\tilde{\mathbf{k}}} \left[\left(D_{ave}^{\alpha\beta}(\mathbf{K}, \omega) \right)^{-1} \right. \\ \left. + \Gamma_{old}^{\alpha\beta}(\mathbf{K}, \omega) - F^{\alpha\beta}(\mathbf{K} + \tilde{\mathbf{k}}) + \bar{F}^{\alpha\beta}(\mathbf{K}) \right]^{-1} \end{aligned} \quad (14)$$

The DCA self-consistency condition requires that the disorder-averaged cluster Green's function equals to the coarse-grained lattice Green's functions, once the convergence is reached

$$\bar{D}^{\alpha\beta}(\mathbf{K}, \omega) = D_{ave}^{\alpha\beta}(\mathbf{K}, \omega) \quad (15)$$

7. A new hybridization function is then obtained using

the updated coarse-grained lattice Green's function

$$\begin{aligned} \Gamma_{new}^{\alpha\beta}(\mathbf{K}, \omega) = \Gamma_{old}^{\alpha\beta}(\mathbf{K}, \omega) + \\ \xi \left(\bar{D}^{\alpha\beta}(\mathbf{K}, \omega) - (D_{ave}^{\alpha\beta}(\mathbf{K}, \omega))^{-1} \right), \end{aligned} \quad (16)$$

here $0 \leq \xi \leq 1$ is a linear mixing parameter used for improving the numerical convergence. We repeat the iteration procedure until the hybridization function converges to the desired numerical accuracy with $\Gamma_{old}^{\alpha\beta}(\mathbf{K}, \omega) = \Gamma_{new}^{\alpha\beta}(\mathbf{K}, \omega)$.

In our analysis to determine the effect of disorder on spectral properties, we use the obtained DCA disorder-averaged Green's function $D_{ave}^{\alpha\beta}(\mathbf{K}, \omega)$ to calculate the arithmetic average density of states (ADOS) for a given phonon branch α as

$$\text{ADOS}^{\alpha\alpha}(\omega^2) = -\frac{2\omega}{N_c \pi} \text{Im} \sum_{\mathbf{K}} \left[D_{ave}^{\alpha\alpha}(\mathbf{K}, \omega^2) \right]. \quad (17)$$

However, as shown in Refs.^{23,43}, the DCA-produced ADOS cannot distinguish between localized and extended states. Being the arithmetically averaged quantity, it always favors the extended state and therefore is not critical at the Anderson transition. To identify the localized state, one then has to resort to the typical medium analysis^{31,44} which we describe in the following section.

D. Typical medium dynamical cluster approximation for phonons

To study the Anderson localization of phonons, one must adopt the typical medium approach in the analysis. It has been demonstrated^{23,43,44} that the typical density of states (TDOS) serves as a suitable order parameter for detecting Anderson-localized states. TDOS vanishes for localized states and remains finite for extended states⁴⁴. In the typical medium approach, the TDOS is approximated using geometric averaging over disorder configurations. Refs.^{23,43,44} show that such geometrically averaged TDOS continuously diminishes as disorder strength approaches the critical point, making it an effective one-particle order parameter for detecting Anderson localization transition.

To incorporate such a typical medium approach into our cluster self-consistency loop, we replace the linearly averaged cluster Green's function $D_{ave}^{\alpha\beta}(L, L', \omega)$ of Eq. 13 with the typical cluster Green's function $D_{typ}^{\alpha\beta}(L, L', \omega)$ obtained from the geometrically averaged density of states. For this purpose, we adopt the same ansatz as in the single-branch case²³ for computing the TDOS (ρ_{typ}), namely

$$\rho_{typ}(\mathbf{K}, \omega) = e^{\frac{1}{N_c} \sum_L \langle \ln \rho_{LL}(\omega) \rangle} \left\langle \frac{\rho(\mathbf{K}, \omega)}{\frac{1}{N_c} \sum_L \rho_{LL}(\omega)} \right\rangle \quad (18)$$

and extend this to the multi-branch case similarly to the multi-branch case for the electron systems³⁴ as:

$$\rho_{typ}^{\alpha\beta}(\mathbf{K}, \omega) = \begin{pmatrix} e^{\frac{1}{N_c} \sum_L \langle \ln \rho_{LL}^{\alpha\alpha}(\omega) \rangle} \left\langle \frac{\rho^{\alpha\alpha}(\mathbf{K}, \omega)}{\frac{1}{N_c} \sum_L \rho_{LL}^{\alpha\alpha}(\omega)} \right\rangle & \dots & e^{\frac{1}{N_c} \sum_L \langle \ln |\rho_{LL}^{\alpha\beta}(\omega)| \rangle} \left\langle \frac{\rho^{\alpha\beta}(\mathbf{K}, \omega)}{\frac{1}{N_c} \sum_L \rho_{LL}^{\alpha\beta}(\omega)} \right\rangle \\ \vdots & & \vdots \\ e^{\frac{1}{N_c} \sum_L \langle \ln |\rho_{LL}^{\beta\alpha}(\omega)| \rangle} \left\langle \frac{\rho^{\beta\alpha}(\mathbf{K}, \omega)}{\frac{1}{N_c} \sum_L \rho_{LL}^{\beta\alpha}(\omega)} \right\rangle & \dots & e^{\frac{1}{N_c} \sum_L \langle \ln \rho_{LL}^{\beta\beta}(\omega) \rangle} \left\langle \frac{\rho^{\beta\beta}(\mathbf{K}, \omega)}{\frac{1}{N_c} \sum_L \rho_{LL}^{\beta\beta}(\omega)} \right\rangle \end{pmatrix}, \quad (19)$$

where

$$\rho_{LL}^{\alpha\beta}(\omega) = -\frac{2\omega}{\pi} \text{Im} D^{\alpha\beta}(L, L, \omega) \quad (20)$$

$$\rho^{\alpha\beta}(\mathbf{K}, \omega) = -\frac{2\omega}{\pi} \text{Im} D^{\alpha\beta}(\mathbf{K}, \omega) \quad (21)$$

are the site local and momentum-dependent spectral functions, respectively, computed from the cluster Green's function of Eq. 11.

From Eq. 19, the disorder-averaged typical cluster Green's function is obtained using the Hilbert transform as

$$D_{typ}^{\alpha\beta}(\mathbf{K}, \omega) = \mathcal{P} \int d\omega' \frac{\rho_{typ}^{\alpha\beta}(\mathbf{K}, \omega')}{\omega^2 - \omega'^2} - i \frac{\pi}{2\omega} \rho_{typ}^{\alpha\beta}(\mathbf{K}, \omega), \quad (22)$$

The rest of the implementation of the multi-branch TMDCA algorithm is very similar to that of the multi-branch DCA of the previous subsection *C*. The only difference is that instead of solving for the algebraically averaged cluster Green's function $D_{ave}^{\alpha\beta}$, one calculates the typical cluster Green's function $D_{typ}^{\alpha\beta}$ using Eq. 22. Once the convergence is reached in the self-consistency loop, we calculate the local TDOS

$$\text{TDOS}^{\alpha\alpha}(\omega^2) = -\frac{2\omega}{N_c \pi} \text{Im} \sum_{\mathbf{K}} \left[D_{typ}^{\alpha\alpha}(\mathbf{K}, \omega) \right]. \quad (23)$$

to analyze the localization of the phonons (see Sec. III).

2.1. Multi-branch force constants model

To simulate the impact of the branch coupling on the localization of phonon, in the following, we first describe the multi-branch force constant model $\Phi^{\alpha\beta}(l, l')$ that we use in our analysis. We consider the force constants between atoms vibrating in three different directions, namely (x, y, z) . For instance, $\Phi^{\alpha\beta}(l, l')$ represents the force constants between atom A at lattice site R_l , which vibrates along the $\alpha(x, y, z)$ direction, and atom B, which vibrates along the $\beta(x, y, z)$ direction. Consequently, the force-constant matrices comprise both diagonal components $\Phi^{\alpha\alpha}(l, l')$, associated with atoms vibrating along the same directions, and off-diagonal components $\Phi^{\alpha\beta}$, associated with atoms vibrating in different directions.

Table-I defines the specific model that we consider in our work. The top three rows of the table, parameter-

Interaction	Value
$\Phi^{\alpha\alpha}(\vec{R}_l, \vec{R}_l)$	-6
$\Phi^{\alpha\alpha}(\vec{R}_l \pm \vec{a}_\alpha, \vec{R}_l)$	$1 + \varepsilon$
$\Phi^{\alpha\alpha}(\vec{R}_l \pm \vec{a}_\beta, \vec{R}_l)$	$1 - \frac{\varepsilon}{2}$
$\Phi^{\alpha\beta}(\vec{R}_l, \vec{R}_l)$	$-6 \times \tau$
$\Phi^{\alpha\beta}(\vec{R}_l \pm \vec{a}_\gamma, \vec{R}_l)$	τ

TABLE I. The force constant model used in our study. $\Phi^{\alpha\beta}(\vec{R}_l, \vec{R}_{l'})$ describes the coupling between the atom at the lattice-site \vec{R}_l vibrating along α direction and the atom at the lattice-site $\vec{R}_{l'}$ vibrating along β direction, where $\alpha, \beta, \gamma \in \{x, y, z\}$, $\alpha \neq \beta$, and \vec{a}_x, \vec{a}_y and \vec{a}_z are the primitive cell cubic lattice vectors.

ized by ε , describes components of the force constant that are diagonal in the branch space, but off-diagonal in the lattice-space. The bottom two rows describes the components that are off-diagonal in the branch basis, which are parametrized by τ . The parameters ε and τ are introduced in such a way that the sum rule is satisfied, i.e., $\sum_l \Phi^{\alpha\beta}(l, l') = 0$.

Notice, that our model recovers the following limited cases. For $\tau = 0$ and $\varepsilon \neq 0$, the model reduces to the trivial case of the system with three decoupled anisotropic branches. When $\tau \neq 0$ and $\varepsilon = 0$, the model also reduces effectively to three decoupled models, each of which rescaled by the eigenvalues of the 3×3 onsite matrix $\Phi^{\alpha\beta}(l, l)$: $1 - \tau, 1 - \tau, 1 + 2\tau$. Importantly, in this case the disorder-induced localization properties of each of these three decoupled models are identical to those of the single-branch model because the eigenvectors of a model are not affected by rescaling the model with an overall constant. Therefore, to investigate a model that is non-equivalent to the single branch case we need to consider $\tau \neq 0$ and $\varepsilon \neq 0$.

III. RESULTS AND DISCUSSIONS

A. Benchmarking of the DCA and ED methods

Since the exact results for the three-directional lattice vibrational model have not been reported in the literature, we have first performed calculations using the exact diagonalization (ED) method. In ED calculations, we adopt the large-size disordered supercells. Within the supercell, the disorder is randomly distributed with

the impurity distributions periodically repeating beyond the supercell boundaries. In ED analysis, we derive the force constant matrices of 100 supercells each with 60 impurities and roughly 400 sites on average for each set of the model parameters. The dynamical matrix of each supercell is then computed and diagonalized on a $10 \times 10 \times 10$ supercell momentum space grid. In our DCA and TMDCA calculations, we consider 1000 disorder realizations for $N_c = 1$ and 100 disorder realization for the cluster size $N_c = 4^3$ on a simple cubic lattice keeping broadening factor $\eta = 10^{-3}$. To test the cluster-size convergence of our results, we have also utilized cluster size $N_c = 5^3$ and verified that our results converge for the clusters beyond $N_c = 4^3$.

We start the discussion of our results by first comparing our developed multi-branch cluster DCA method with the ED results for a binary isotopic alloy system in three dimensions. This benchmarking analysis aims to evaluate the accuracy and effectiveness of our developed multi-branch cluster DCA approach in capturing the system's behavior. For this, in Fig. 1, we compare the average density of states (ADOS) calculated for an impurity concentration of $c_A = 0.2$ and a disorder potential of $V = 0.9$, for a fixed value of $\tau = 0.3$ and varying values of ε . First, on panel Fig. 1-a), we consider the case of $\varepsilon = 0.0$, where we compare the DCA and ED results, and observe a perfect agreement between two methods. For the finite values of τ , we anticipate the emergence of two impurity modes in the higher frequency regions. Specifically, we expect a doubly degenerate impurity band at the lower end of the high-frequency region and a single impurity band at the higher end, corresponding to the eigenvalues of the 3×3 onsite matrix $\Phi^{\alpha\beta}(l, l)$: $1 - \tau, 1 - \tau, 1 + 2\tau$ as explained in section II. As shown in Fig. 1, the two impurity modes around frequency regions $2 < \omega < 4$ and $4 < \omega < 6$ are well captured by our DCA method and are in perfect agreement with the ED results.

To evaluate the effects of non-local spatial correlations, Fig. 1-b) compares the ADOS obtained with the local CPA method, corresponding to the $N_c = 1$ DCA case, against the exact ED data. Although the CPA method approximately reproduces the overall shape of the exact ADOS, it fails to capture the fine-structure features of the impurity modes, especially in the high-frequency region. This discrepancy is anticipated and well-understood due to the single-site nature of the CPA method, which cannot capture the non-local spatial correlations present in the system, leading to significant structures in the ADOS. These results underscore the importance of non-local spatial correlations, absent in the local CPA method, but accounted for in the finite cluster DCA.

Next, we proceed to compare our multi-branch DCA results against ED data for a finite value of ε . This corresponds to a scenario where atomic vibrations at site R_l in the α directions are coupled with atomic vibrations around $R_{l'}$ in the β directions by the tuning parameter ε . Fig. 1-c) and Fig. 1-d) show the results for $\varepsilon = 0.2$ and

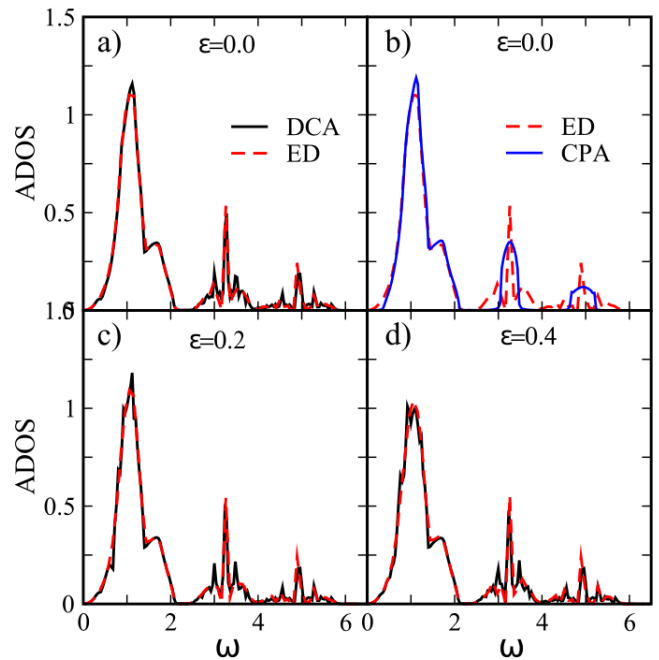


FIG. 1. Parameters: $\tau = 0.3, c_A = 0.2, V_A = 0.9$. A comparison of the ADOS obtained by the developed multi-branch DCA, single site CPA and the exact diagonalization method (ED). Panel a) shows the ADOS obtained from the multi-branch DCA using a cluster size of $N_c = 4^3$ and the ED results for $\varepsilon = 0$. Panel b) compares the single-site CPA results with ED results for $\varepsilon = 0$. Note that, unlike the DCA, the CPA fails to reproduce the fine-structure features of the high-frequency impurity mode of the ADOS as found in exact calculations. Panels c) and d) show the multi-branch DCA results for the case where the atomic vibrations at lattice site R_l in the direction α are coupled with atomic vibrations around $R_{l'}$ in the direction β by the tuning parameter ε of 0.2 and 0.4, respectively. It is observed that the host mode height changes with increasing ε , and the multi-branch DCA results are in strong agreement with the ED results.

$\varepsilon = 0.4$, respectively. While there is no significant difference in the high-frequency impurity modes, it is observed that the height of the host mode decreases with increasing ε values. Our multi-branch DCA method successfully captures all the fine features of the ADOS, as evidenced by the remarkable agreement with ED data for a binary alloy. As presented in Appendix A, we have also explored other disorder distributions, such as uniform distributions, and found excellent agreement between the multi-branch DCA results and ED results. These findings demonstrate the efficiency of our developed multi-branch DCA scheme in computing the average phonon density of states for complex systems.

It is worth noting that we have verified the convergence of our results with respect to the cluster size N_c . We found that the results obtained for $N_c = 4^3$ and $N_c = 5^3$ are practically identical, which establishes that our data converges very quickly to the exact thermodynamic

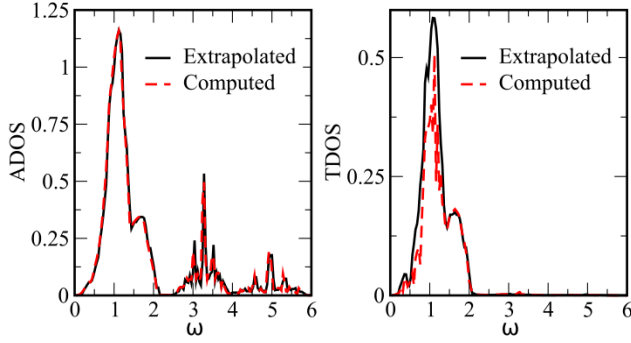


FIG. 2. Parameters: $\tau = 0.3, \varepsilon = 0.0, c_A = 0.2, V_A = 0.9$. Left panel: comparison of the ADOS obtained from Eq. 24 and from the multi-branch DCA formalism. Right panel: comparison of the TDOS obtained from Eq. 25 and the multi-branch TMDCA formalism.

limit. This highlights the efficiency of the DCA $N_c = 4^3$ cluster in capturing the essential physics of complex systems while keeping computational costs reasonable.

B. $\varepsilon = 0$ and $\tau \neq 0$: branch-decoupled case

As discussed in Section II, our multi-branch model simplifies to three decoupled single-branch models when $\varepsilon = 0$ and $\tau \neq 0$. Under these conditions, the total average density of states (ADOS) of the multi-branch model, can be obtained from the average density of states of a single branch, $\text{ados}(\omega)$ as follows (see Appendix B for the details):

$$\text{ADOS}(\omega) = \sum_m \text{ados}\left(\frac{\omega}{\sqrt{\varepsilon_m}}\right), \quad (24)$$

where ε_m are the eigenvalues of the 3×3 onsite matrix $\Phi^{\alpha\beta}(l, l)$, equal to $1 - \tau, 1 - \tau, 1 + 2\tau$, respectively.

To validate these results, Fig. 2 (left panel) presents the ADOS obtained via DCA (computed) and the ADOS extrapolated from the single-branch density of states using Eq. 24 for the case where $\varepsilon = 0$ and $\tau = 0.3$. As observed in the figure, there is an excellent agreement between the results.

Naively, one might expect that a similar extrapolation formula exists for the typical medium case, wherein the total multi-branch TDOS(ω) is related to the typical density of states, $\text{tdos}(\omega)$, of an individual branch in a manner similar to that observed for the average case (see Appendix B for further details)

$$\text{TDOS}(\omega) = \sum_m \text{tdos}\left(\frac{\omega}{\sqrt{\varepsilon_m}}\right) \quad (25)$$

However, as seen from Fig. 2 (right panel), the TDOS(ω) extrapolated from the $\text{tdos}(\omega)$ of a single branch, using Eq. 25 only approximately agrees with the

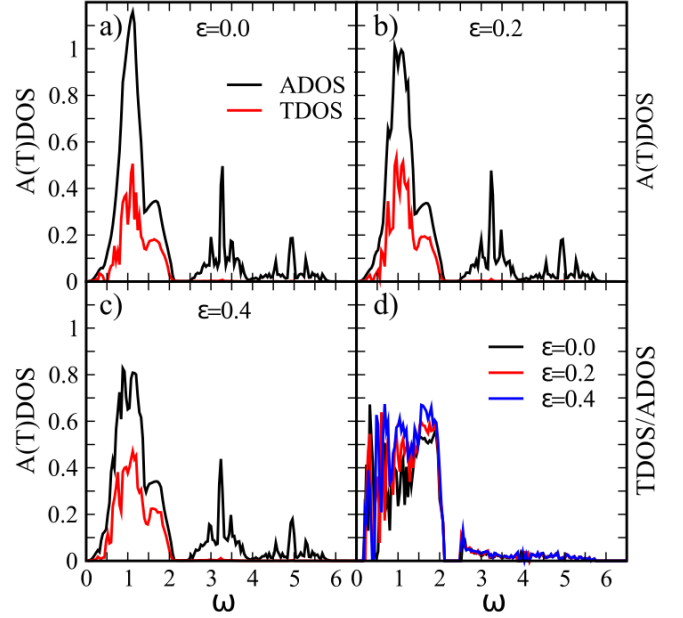


FIG. 3. Parameters: $\tau = 0.3, c_A = 0.2, V_A = 0.9, N_c = 4^3$. Panels a), b), and c) show the evolution of the average ADOS and the typical TDOS for increasing values of $\varepsilon = 0, 0.2, 0.4$ at at large disorder ($V_A = 0.9$) and small impurity concentration $c_A = 0.2$. Panel d) shows the ratio of TDOS/ADOS for all values of $\varepsilon = 0, 0.2, 0.4$.

TDOS computed directly from the multi-branch model using the TMDCA. In Appendix B, we detail why Eq. 25 is not universally valid.

C. $\varepsilon \neq 0$ and $\tau \neq 0$: inter-branch coupling case

In this section, we investigate the localization of phonons in our mass-disordered multi-branch model in the case where the inter-branch coupling occurs and the system is not equivalent to the single-branch model. This corresponds to the case with $\varepsilon \neq 0$ and $\tau \neq 0$.

In Fig. 3, to demonstrate the impact of inter-branch coupling on phonon localization, we plot the ADOS and TDOS for increasing values of $\varepsilon = 0.0, 0.2, 0.4$ at a fixed disorder potential $V_A = 0.9$ and small impurity concentration of $c_A = 0.2$. Beginning with the branch-decoupled case ($\varepsilon = 0.0$), as shown in Fig. 3-a), we observe strong localization for high-frequency phonon modes within the frequency range of $\omega = 2.5$ to $\omega = 6.0$. This is evident from the TDOS approaching zero while the ADOS remains finite. The results for finite $\varepsilon = 0.2$ and $\varepsilon = 0.4$ are shown in Fig. 3-b) and Fig. 3-c). The data indicate a negligible effect of ε on the localized phonons, although subtle changes are observed in the host modes. Specifically, the host mode becomes slightly broader and more delocalized with increasing ε . However, high-frequency phonons remain localized even as ε increases. This is clearly illustrated in Fig. 3-d), where

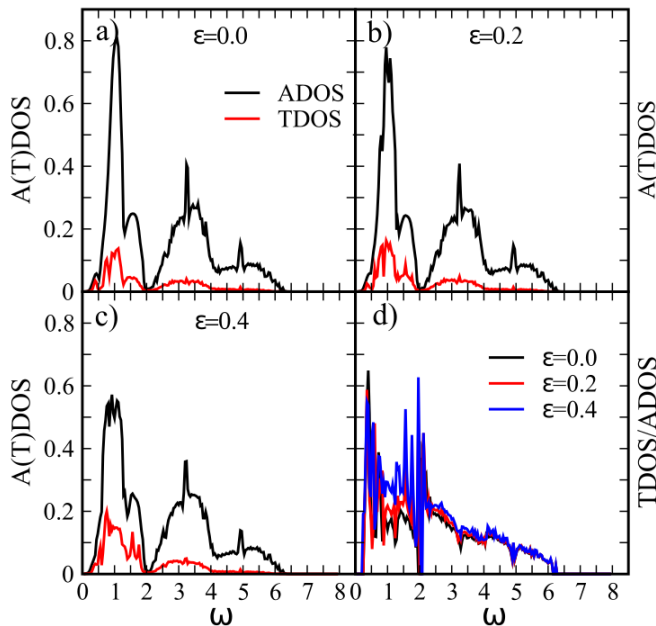


FIG. 4. Parameters: $\tau = 0.3, c_A = 0.5, V_A = 0.9, N_c = 4^3$. Panels a), b), and c) show the evolution of the average ADOS and the typical TDOS for increasing values of $\varepsilon = 0, 0.2, 0.4$ at large disorder ($V_A = 0.9$) and moderate impurity concentration ($c = 0.5$). d) the TDOS/ADOS ratio at $\varepsilon = 0.0, 0.2, 0.4$.

the ratio of TDOS/ADOS remains nearly constant across the range of considered ε values (0 to 0.4).

Next, we consider an opposite scenario where we start with the impurity modes being delocalized, which occurs at higher impurity concentration at $c_A = 0.5$ and $V_A = 0.9, \varepsilon = 0.0, 0.2, 0.4$. In this case, as seen from Fig. 4-a) the impurity phonon modes are delocalized around $\omega = 2$ to 4.5 as depicted by a finite TDOS within this region. Our goal is to understand how ε affects these delocalized phonons. As seen from Fig. 4-b) and Fig. 4-c), the delocalized phonons remain delocalized even when ε is increased from 0 to 0.4, although there are subtle changes in the mid-frequency region of the spectrum. We confirm this observation by examining the ratio of TDOS/ADOS, which remains almost unchanged as shown in Fig. 4-d).

Finally, to further illustrate this effect, in Fig. 5, we examine a case with a highly delocalized spectrum which occurs at low disorder potential $V_A = 0.5$. For such case, we observe that ADOS and TDOS are both finite across the entire frequency range for increasing values of ε , with the delocalized phonon spectrum being concentrated in the mid-frequency region for all values ε . Notably, while the TDOS shape shifts with increasing ε , the phonon modes remain delocalized. This is further confirmed by the near-constant ratio of TDOS/ADOS in Fig. 5-d), indicating minimal impact of ε on phonon localization. Therefore, a low disorder potential favors highly delocalized phonon modes unaffected by ε changes.

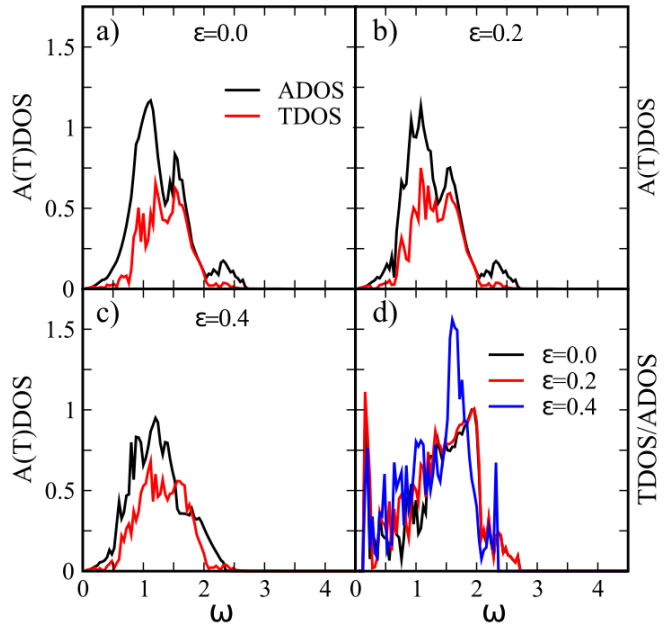


FIG. 5. Parameters: $\tau = 0.3, c_A = 0.2, V_A = 0.5, N_c = 4^3$. Panels (a), (b), and (c) show the evaluation of ADOS and TDOS and with increasing ε values from 0 to 0.2 to 0.4 at intermediate disorder strength ($V_A = 0.5$). (d) the TDOS/ADOS ratio at $\varepsilon = 0.0, 0.2, 0.4$

IV. CONCLUSIONS

In our study, we have introduced the multi-branch DCA and TMDCA formalisms to investigate the effects of disorder on the phonon spectrum in multi-branch systems. By comparing our results with exact ED results, we have found excellent agreement between the developed multi-branch DCA formalism and spectral functions for both binary and box disorder distributions. We have demonstrated the importance of the cluster extension of a single-site local CPA approximation to avoid averaging out essential non-local features in the spectrum. Although cluster DCA has advantages in incorporating non-local spatial correlations, it fails to capture Anderson localization due to the arithmetic averaging over disorder configurations. To address this limitation, we have developed the TMDCA multi-branch formalism, where a typical averaging ansatz replaces the arithmetic averaging in the self-consistency loop. Using the typical density of states as the order parameter for Anderson localization, we have investigated the impact of various vibrational multi-branch couplings (τ and ε) on phonon localization. Our study reveals that the multi-branch couplings in the model investigated have little effect on the Anderson transition of phonon localization in the presence of mass disorder. Specifically, our results demonstrate that localized states remain localized and extended states remain extended, largely regardless of the value of τ and ε . This does not rule out that multi-branch couplings in

other models could be important for the localization of phonons. We leave, that question for future studies.

In summary, our study demonstrates that the developed multi-branch DCA and TMDCA methods are computationally efficient, able to capture exact results even at a small cluster size of $N_c = 4^3$, and are fully causal. The DCA is effective in capturing non-local spatial correlations and other fine features in the DOS, while the TMDCA can address the key aspects of the Anderson localization of phonons caused by the complex force-constants model. Therefore, the developed multi-branch cluster approach is a promising tool for investigating phonon localization in real materials. Furthermore, as Green's function approach, the multi-branch TMDCA can be readily applied to a range of layered geometries, superlattice structures, heterostructures, thin films, and interfaces.

ACKNOWLEDGMENTS

HT and WM acknowledge support by NSF DMR-1944974 grant. This work used Expanse at SDSC through allocation DMR 130036 from the Advanced Cyberinfrastructure Coordination Ecosystem: Services & Support (ACCESS) program, which is supported by National Science Foundation grants #2138259, #2138286, #2138307, #2137603, and #2138296. This research also used resources of the Oak Ridge Leadership Computing Facility, which is a DOE Office of Science User Facility supported under Contract DE-AC05-00OR22725. A portion of this research (TB) was conducted at the Center for Nanophase Materials Sciences, which is a Department of Energy (DOE) Office of Science User Facility. In addition, we used resources of the National Energy Research Scientific Computing Center, a DOE Office of Science User Facility supported by the Office of Science of the U.S. DOE under Contract No. DE-AC02-05CH11231.

Appendix A: Comparison of the DCA and ED for the uniform (box) disorder distribution

To demonstrate the generalizability of our multi-branch DCA method, we compared its performance with exact diagonalization (ED) results for a uniform "box" disorder distribution ($P(V) = \frac{1}{W}\Theta(|V - W/2|)$). The left panel of Fig. 6 (a-b) shows the comparison for the case of $\tau = 0$, whereas the right panel (c-d) shows the comparison for finite values of $\tau = 0.5, 0.9$. In both cases, we find excellent agreement with the exact ED results, indicating the validity of our multi-branch DCA method for arbitrary values of τ and strength of disorder W in the case of uniform disorder distribution.

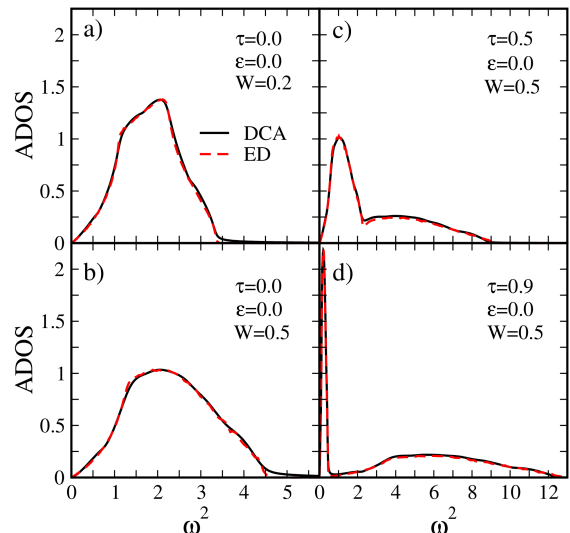


FIG. 6. A comparison of the ADOS obtained from the multi-branch DCA using a cluster size of $N_c = 4^3$ with the exact diagonalization method (ED) for the uniform (box) disorder distribution.

Appendix B: $\varepsilon = 0$ and $\tau \neq 0$: branch-decoupled case

Average medium case: Suppose that in the N_b -branch force constant matrix, the branch and lattice degrees of freedom are decoupled as follows:

$$\Phi_{N_b}^{\alpha\beta}(l, l') = K_1(l, l')M(\alpha, \beta), \quad (\text{B1})$$

here, l and α denote the lattice and branch indices, respectively. $K_1(l, l')$ represents a single-branch force constant matrix in lattice-space, while $M(\alpha, \beta)$ is a $N_b \times N_b$ force constant matrix in the branch space, the latter with eigenvalues ε_m . In this case, we can show that the total multi-branch density of states, denoted as $\text{ADOS}(\omega)$, is related to the single-branch density of states, $\text{ados}(\omega)$, and the eigenvalues ε_m , as follows:

$$\text{ADOS}(\omega) = \sum_m \frac{1}{\sqrt{\varepsilon_m}} \text{ados}\left(\frac{\omega}{\sqrt{\varepsilon_m}}\right) \quad (\text{B2})$$

Below, we provide the derivation of Eq. B2. The eigenvalues E_J of $\Phi_{N_b}^{\alpha\beta}$ are related to the eigenvalues ε_j of the K_1 matrix and ε_m of the M matrix as $E_J = \varepsilon_m \varepsilon_j$. The corresponding eigenvectors of $\Phi_{N_b}^{\alpha\beta}(l, l')$ are given by $\phi_J(l, \alpha) = \psi_j(l)\gamma_m(\alpha)$, where $\psi_j(l)$ is the eigenvector of the single-branch K_1 matrix, and $\gamma_m(\alpha)$ is the eigenvector of the force constant matrix M in branch space.

From here, we observe that the multi-branch density

of states $DOS(\omega, l)$ at site l is given by:

$$\begin{aligned}
DOS(\omega, l) &= \sum_{\alpha, J} \phi_J(l, \alpha) \phi_J^*(l, \alpha) \delta(\omega - \sqrt{E_J}) \\
&= \sum_{\alpha, m, j} \psi_j(l) \gamma_m(\alpha) \psi_j^*(l) \gamma_m^*(\alpha) \delta(\omega - \sqrt{\varepsilon_m \varepsilon_j}) \\
&= \sum_{m, j} \psi_j(l) \psi_j^*(l) \frac{1}{\sqrt{\varepsilon_m}} \delta\left(\frac{\omega}{\sqrt{\varepsilon_m}} - \sqrt{\varepsilon_j}\right) \\
&= \sum_m \frac{1}{\sqrt{\varepsilon_m}} \text{dos}\left(\frac{\omega}{\sqrt{\varepsilon_m}}, l\right) \tag{B3}
\end{aligned}$$

where we used the completeness of the branch space with $\sum_{\alpha} \gamma_m^*(\alpha) \gamma_m(\alpha) = 1$, and that $\text{dos}(\frac{\omega}{\sqrt{\varepsilon_m}}, l) = \sum_j \psi_j(l) \psi_j^*(l) \delta(\frac{\omega}{\sqrt{\varepsilon_m}} - \sqrt{\varepsilon_j})$ is the single-branch local density of states at site l .

Hence, we can deduce that the local multi-branch density of states, $ADOS(\omega)$, can be written as

$$\begin{aligned}
ADOS(\omega) &= \frac{1}{N_l} \sum_l DOS(\omega, l) \\
&= \sum_m \frac{1}{\sqrt{\varepsilon_m}} \left(\frac{1}{N_l} \sum_l \text{dos}\left(\frac{\omega}{\sqrt{\varepsilon_m}}, l\right) \right) \\
&= \sum_m \text{ados}\left(\frac{\omega}{\sqrt{\varepsilon_m}}\right), \tag{B4}
\end{aligned}$$

where $\text{ados}(\frac{\omega}{\sqrt{\varepsilon_m}}) = \frac{1}{\sqrt{\varepsilon_m}} \left(\frac{1}{N_l} \sum_l \text{dos}\left(\frac{\omega}{\sqrt{\varepsilon_m}}, l\right) \right)$ is the average density of states of the single branch.

Typical medium case: In the following, we show that, in general, there is no simple relation for the total typical density of states case for multi-branch systems, unlike the relation (Eq. B4) for the average density of states case. To illustrate this, let's consider a case with two lattice sites and two branches. Using the geometric averaging to calculate the typical DOS, with $\text{TDOS}(\omega) = \left(\prod_l DOS(\omega, l) \right)^{\frac{1}{N_l}}$, we obtain $\text{TDOS}(\omega) =$

$(DOS(\omega, l_1) DOS(\omega, l_2))^{1/2}$. Substituting in the expression for the $DOS(\omega, l)$ from Eq. B3, we have

$$\begin{aligned}
\text{TDOS}(\omega) &= [DOS(\omega, l_1) DOS(\omega, l_2)]^{1/2} \\
&= \left[\left(\frac{1}{\sqrt{\varepsilon_1}} \text{dos}\left(\frac{\omega}{\sqrt{\varepsilon_1}}, l_1\right) + \frac{1}{\sqrt{\varepsilon_2}} \text{dos}\left(\frac{\omega}{\sqrt{\varepsilon_2}}, l_1\right) \right) \right. \\
&\quad \times \left. \left(\frac{1}{\sqrt{\varepsilon_1}} \text{dos}\left(\frac{\omega}{\sqrt{\varepsilon_1}}, l_2\right) + \frac{1}{\sqrt{\varepsilon_2}} \text{dos}\left(\frac{\omega}{\sqrt{\varepsilon_2}}, l_2\right) \right) \right]^{1/2} \\
&= \left[\frac{1}{\sqrt{\varepsilon_1}} \frac{1}{\sqrt{\varepsilon_1}} \text{dos}\left(\frac{\omega}{\sqrt{\varepsilon_1}}, l_1\right) \text{dos}\left(\frac{\omega}{\sqrt{\varepsilon_1}}, l_2\right) \right. \\
&\quad + \frac{1}{\sqrt{\varepsilon_1}} \frac{1}{\sqrt{\varepsilon_2}} \text{dos}\left(\frac{\omega}{\sqrt{\varepsilon_1}}, l_1\right) \text{dos}\left(\frac{\omega}{\sqrt{\varepsilon_2}}, l_2\right) \\
&\quad + \frac{1}{\sqrt{\varepsilon_2}} \frac{1}{\sqrt{\varepsilon_1}} \text{dos}\left(\frac{\omega}{\sqrt{\varepsilon_2}}, l_1\right) \text{dos}\left(\frac{\omega}{\sqrt{\varepsilon_1}}, l_2\right) \\
&\quad \left. + \frac{1}{\sqrt{\varepsilon_2}} \frac{1}{\sqrt{\varepsilon_2}} \text{dos}\left(\frac{\omega}{\sqrt{\varepsilon_2}}, l_1\right) \text{dos}\left(\frac{\omega}{\sqrt{\varepsilon_2}}, l_2\right) \right]^{1/2} \tag{B5}
\end{aligned}$$

Now, considering that the typical density of states of an individual branch is defined as $\text{tdos}(\omega/\sqrt{\varepsilon_m}) = \left(\prod_l \frac{1}{\sqrt{\varepsilon_m}} \text{dos}(\omega/\sqrt{\varepsilon_m}, l) \right)^{1/N_l}$, we can rewrite Eq. B5 as

$$\text{TDOS}(\omega) = \left(\sum_m \text{tdos}^2(\omega/\sqrt{\varepsilon_m}) + \text{cross terms} \right)^{1/2}. \tag{B6}$$

This in general is not equal to the typical density of states analogy of Eq. B4:

$$\text{TDOS}(\omega) = \sum_m \text{tdos}(\omega/\sqrt{\varepsilon_m}) \tag{B7}$$

with $\text{tdos}(\omega/\sqrt{\varepsilon_m}) = \left(\prod_l \frac{1}{\sqrt{\varepsilon_m}} \text{dos}(\omega/\sqrt{\varepsilon_m}, l) \right)^{1/N_l}$. Note, that this equation holds for the N_b multi-branch case with N_l sites.

* hanna.teletskia@mtsu.edu

¹ P. W. Anderson, Phys. Rev. **109**, 1492 (1958).

² B. Kramer, G. Bergmann, and Y. Bruynseraede, *Localization, Interaction, and Transport Phenomena: Proceedings of the International Conference, August 23–28, 1984 Braunschweig, Fed. Rep. of Germany*, Vol. 61 (Springer Science & Business Media, 2012).

³ E. Abrahams, P. W. Anderson, D. C. Licciardello, and T. V. Ramakrishnan, Phys. Rev. Lett. **42**, 673 (1979).

⁴ D. Vollhardt and P. Wölfle, Phys. Rev. Lett. **48**, 699 (1982).

⁵ S. John, H. Sompolinsky, and M. J. Stephen, Phys. Rev. B **27**, 5592 (1983).

⁶ Y. Ni and S. Volz, Journal of Applied Physics **130** (2021), 10.1063/5.0073129.

⁷ Z. Tian, ACS Nano **13**, 3750 (2019).

⁸ M. H. Lee, J. H. Yun, G. Kim, J. E. Lee, S.-D. Park, H. Reith, G. Schierning, K. Nielsch, W. Ko, A.-P. Li, and J.-S. Rhyee, ACS Nano **13**, 3806 (2019).

⁹ S. Xiong, K. Säskilähti, Y. A. Kosevich, H. Han, D. Donadio, and S. Volz, Phys. Rev. Lett. **117**, 025503 (2016).

¹⁰ H. Yang, B. Jia, L. Xie, D. Mao, J. Xia, J. Yang, M. Yuan, Q. Gan, X. Liu, M. Hu, J. Shuai, and J. He, Joule (2024), <https://doi.org/10.1016/j.joule.2024.06.020>.

¹¹ M. E. Manley, P. J. Stonaha, N. M. Bruno, I. Karaman, R. Arroyave, S. Chi, D. L. Abernathy, M. B. Stone, Y. I. Chumlyakov, and J. W. Lynn, Science Advances **10**, eadn2840 (2024), <https://www.science.org/doi/pdf/10.1126/sciadv.adn2840>.

¹² D. Ma, X. Li, and L. Zhang, Chinese Physics B **29**, 126502 (2020).

¹³ R. Hu, S. Iwamoto, L. Feng, S. Ju, S. Hu, M. Ohnishi,

- N. Nagai, K. Hirakawa, and J. Shiomi, *Phys. Rev. X* **10**, 021050 (2020).
- ¹⁴ C. Monthus and T. Garel, *Phys. Rev. B* **81**, 224208 (2010).
- ¹⁵ M. N. Luckyanova, J. Mendoza, H. Lu, B. Song, S. Huang, J. Zhou, M. Li, Y. Dong, H. Zhou, J. Garlow, L. Wu, B. J. Kirby, A. J. Grutter, A. A. Puretzy, Y. Zhu, M. S. Dresselhaus, A. Gossard, and G. Chen, *Science Advances* **4**, eaat9460 (2018), <https://www.science.org/doi/pdf/10.1126/sciadv.aat9460>.
- ¹⁶ M. E. Manley, J. W. Lynn, D. L. Abernathy, E. D. Specht, O. Delaire, A. R. Bishop, R. Sahul, and J. D. Budai, *Nature Communications* **5**, 3683 EP (2014), article.
- ¹⁷ R. T. Howie, I. B. Magdău, A. F. Goncharov, G. J. Ackland, and E. Gregoryanz, *Phys. Rev. Lett.* **113**, 175501 (2014).
- ¹⁸ S. Faez, A. Strybulevych, J. H. Page, A. Lagendijk, and B. A. van Tiggelen, *Phys. Rev. Lett.* **103**, 155703 (2009).
- ¹⁹ H. Hu, A. Strybulevych, J. H. Page, S. E. Skipetrov, and B. A. van Tiggelen, *Nature Physics* **4**, 945 EP (2008).
- ²⁰ H. A. H. Z. R. S. C. P. J. Islam, Md. Sherajul and A. Hashimoto, *ACS Omega* (2022), 10.1021/acsomega.2c02792.
- ²¹ S. E. Skipetrov and I. M. Sokolov, *Phys. Rev. Lett.* **112**, 023905 (2014).
- ²² S. E. Skipetrov and Y. M. Beltukov, *Phys. Rev. B* **98**, 064206 (2018).
- ²³ W. R. Mondal, N. S. Vidhyadhiraja, T. Berlijn, J. Moreno, and M. Jarrell, *Phys. Rev. B* **96**, 014203 (2017).
- ²⁴ T. R. Kirkpatrick, *Phys. Rev. B* **31**, 5746 (1985).
- ²⁵ D. N. Payton and W. M. Visscher, *Phys. Rev.* **154**, 802 (1967).
- ²⁶ J. J. Ludlam, S. N. Taraskin, and S. R. Elliott, *Phys. Rev. B* **67**, 132203 (2003).
- ²⁷ S. D. Pinski, W. Schirmacher, and R. A. Römer, *EPL (Europhysics Letters)* **97**, 16007 (2012).
- ²⁸ P. Soven, *Phys. Rev.* **156**, 809 (1967).
- ²⁹ R. J. Elliott, J. A. Krumhansl, and P. L. Leath, *Rev. Mod. Phys.* **46**, 465 (1974).
- ³⁰ M. Jarrell and H. R. Krishnamurthy, *Phys. Rev. B* **63**, 125102 (2001).
- ³¹ C. E. Ekuma, H. Terletska, K.-M. Tam, Z.-Y. Meng, J. Moreno, and M. Jarrell, *Phys. Rev. B* **89**, 081107 (2014).
- ³² H. Terletska, C. E. Ekuma, C. Moore, K.-M. Tam, J. Moreno, and M. Jarrell, *Phys. Rev. B* **90**, 094208 (2014).
- ³³ C. E. Ekuma, C. Moore, H. Terletska, K.-M. Tam, J. Moreno, M. Jarrell, and N. S. Vidhyadhiraja, *Phys. Rev. B* **92**, 014209 (2015).
- ³⁴ Y. Zhang, H. Terletska, C. Moore, C. Ekuma, K.-M. Tam, T. Berlijn, W. Ku, J. Moreno, and M. Jarrell, *Phys. Rev. B* **92**, 205111 (2015).
- ³⁵ Y. Zhang, R. Nelson, E. Siddiqui, K.-M. Tam, U. Yu, T. Berlijn, W. Ku, N. S. Vidhyadhiraja, J. Moreno, and M. Jarrell, *Phys. Rev. B* **94**, 224208 (2016).
- ³⁶ K.-M. Tam, H. Terletska, T. Berlijn, L. Chioncel, and J. Moreno, *Crystals* **11**, 1282 (2021).
- ³⁷ S. Ghosh, P. L. Leath, and M. H. Cohen, *Phys. Rev. B* **66**, 214206 (2002).
- ³⁸ I. B. Magdău and G. J. Ackland, *Phys. Rev. Lett.* **118**, 145701 (2017).
- ³⁹ J. Zhang, H. Zhang, Q. Wang, W. Sun, and D. Zhang, *Coatings* **12** (2022), 10.3390/coatings12040422.
- ⁴⁰ Y. Zhang, Y. F. Zhang, S. X. Yang, K.-M. Tam, N. S. Vidhyadhiraja, and M. Jarrell, *Phys. Rev. B* **95**, 144208 (2017).
- ⁴¹ T. Maier, M. Jarrell, T. Pruschke, and M. H. Hettler, *Rev. Mod. Phys.* **77**, 1027 (2005).
- ⁴² A. Georges, G. Kotliar, W. Krauth, and M. J. Rozenberg, *Rev. Mod. Phys.* **68**, 13 (1996).
- ⁴³ H. Terletska, A. Moilanen, K.-M. Tam, Y. Zhang, Y. Wang, M. Eisenbach, N. Vidhyadhiraja, L. Chioncel, and J. Moreno, *Annals of Physics* **435**, 168454 (2021), special Issue on Localisation 2020.
- ⁴⁴ V. Dobrosavljević, A. A. Pastor, and B. K. Nikolić, *Europhysics Letters* **62**, 76 (2003).